Nanoscale

PAPER

View Article Online
View Journal | View Issue

Cite this: *Nanoscale*, 2025, **17**, 11679

Stability of multifunctional Pd–Rh electrocatalysts supported on Co_3O_4(111) in alkaline environment: impact of the electronic metal–support interaction†

Alexander Simanenko, [a] Jan Škvára,[b] Pankaj Kumar Samal, [b] Evanie Franz, [a] Robert Hübsch, [a] Tomáš Skála, [b] Nataliya Tsud, [b] Sascha Mehl, [c] Daniel Schauermann, [a] Viktor Johánek, [b] Josef Mysliveček, [b] Olaf Brummel, [a] Yaroslava Lykhach *[a] and Jörg Libuda [a]

The stabilities of monometallic Rh and Pd nanoparticles and bimetallic Pd–Rh core–shell nanoparticles supported on Co_3O_4(111) thin films grown on Ir(100) were investigated with respect to the oxidation state and dissolution in alkaline electrolyte under the conditions relevant for electrochemical ethanol oxidation. Towards this aim, the well-defined model systems were characterized by means of synchrotron radiation photoelectron spectroscopy coupled with an *ex situ* emersion electrochemical cell (EC-SRPES) and scanning tunneling microscopy (STM). We found that the electronic metal–support interaction (EMSI) has a strong influence on the oxidation state of Rh, resulting in a strong oxidation and anchoring of the oxidized Rh^{3+} species on the surface of Co_3O_4(111). Consequently, the EMSI prevents the dissolution of Rh into the electrolyte regardless of the potential range. In contrast, it has no effect on the oxidation state and dissolution of Pd in the potential range of 0.3–1.1 V_{RHE}. However, extending the potential range to 0.3–1.5 V_{RHE} results in a stronger dissolution of Pd due to the reversible oxidation/reduction of Pd, which is enhanced in the presence of the EMSI. Most importantly, the magnitude of the EMSI and, thus, the extent of noble metal oxidation, can be effectively controlled by the nature of the metal/Co_3O_4(111) interface in the bimetallic Pd–Rh core–shell nanoparticles.

Received 28th January 2025,
Accepted 11th April 2025

DOI: 10.1039/d5nr00413f

rsc.li/nanoscale

Introduction

Recent advances in the development of alkaline anion exchange membranes[1–3] and smart catalyst designs[4–6] significantly boosted the performance of alkaline direct alcohol fuel cells. In particular, direct ethanol fuel cells (DEFCs) gained the potential to compete with both fossil fuels and electric batteries as a source of energy for automotive applications.[7,8] Key benefits of DEFCs include low toxicity, zero net carbon emissions, and no recharging times.[8] Pd-based materials are the most active catalysts for alkaline DEFCs.[9,10] The integration of Pd with other metals has been shown to improve catalytic performance through geometric and electronic effects induced by nanostructuring, tensile strain, and interatomic orbital hybridization.[11–15] Most recently, Rh-based nanostructures enriched with low-coordinated sites demonstrated excellent selectivity for complete ethanol oxidation to CO_2.[16,17] Potentially, bimetallic Pd–Rh compounds gain multifunctional properties associated with C–C bond cleavage and supply of active oxygen species (such as OH^-) for efficient ethanol oxidation and removal of carbonaceous residues.[18–20] Still, the electrochemical stability of complex multifunctional catalysts under operating conditions is one of the major challenges.[21–24] The aggregation, dissolution, and restructuring of the noble metal nanoparticles during prolonged electrochemical cycles undermines the efficiency and durability of the catalysts.[25–27] To address these issues, reducible oxide supports such as

[a]*Interface Research and Catalysis, ECRC, Friedrich-Alexander-Universität Erlangen-Nürnberg, Egerlandstraße 3, 91058 Erlangen, Germany.*
E-mail: yaroslava.lykhach@fau.de
[b]*Charles University, Faculty of Mathematics and Physics, Department of Surface and Plasma Science, V Holešovičkách 2, Prague, 18000, Czech Republic*
[c]*Elettra-Sincrotrone Trieste SCpA, Strada Statale 14, km 163.5, Basovizza-Trieste, 34149, Italy*

†Electronic supplementary information (ESI) available: Fitting parameters for Pd 3d and Rh 3d core levels, STM image of Co_3O_4(111) film, Pd 3d spectra obtained from Pd/Co_3O_4(111) using different photon energies; analysis of dissolution and carbon deposition after CV series, validation of the method, Python script, Co 2p and O 1s obtained from Pd/Co_3O_4(111), Rh/Co_3O_4(111), Rh@Pd/Co_3O_4(111), and Pd@Rh/Co_3O_4(111); IMFPs of Rh 3d and Pd 3d photoelectrons in Pd, Rh, and Co_3O_4 excited with different photon energies; analysis of the depth distribution of Rh species in Rh/Co_3O_4(111), Rh@Pd/Co_3O_4(111), and Pd@Rh/Co_3O_4(111). See DOI: https://doi.org/10.1039/d5nr00413f

Co_3O_4 have attracted attention for stabilizing the metal nanoparticles.[28–30] The effect is essentially caused by the electronic metal–support interaction (EMSI) associated with the charge transfer across the metal/oxide interface.[28–31] The EMSI has a strong influence on the morphology and chemical state of both monometallic Pd and Rh nanoparticles supported on Co_3O_4(111).[32,33] However, the role of the EMSI in stabilizing the bimetallic Pd–Rh core–shell nanostructures is rather complex. Recently, we found that the EMSI has the strongest impact on Rh and leads to partial atomic dispersion followed by diffusion of Rh into Co_3O_4(111). However, EMSI has essentially no effect on the atomic ordering in the core–shell nanostructures.[33] Eventually, Rh bulk diffusion leads to the collapse of the core–shell nanostructure and phase separation yielding Rh-rich and Pd-rich nanoparticles upon annealing in ultrahigh vacuum.[33] It is not clear, however, to which extent these phenomena impact the stability of the Pd–Rh core–shell nanoparticles under electrochemical conditions.

Based on our recent study, the oxidation state and stability of the monometallic Pd/Co_3O_4(111) system in alkaline environment is strongly influenced by the size and the shape of Pd nanoparticles that are directly controlled by the EMSI.[34] In the limit of small Pd nanoparticles, a larger magnitude of the EMSI leads to stronger dissolution. This effect is suppressed for Pd nanoparticles thicker than one atomic layer.[34] The benefit of the EMSI for the Pd/Co_3O_4(111) system is a shift of the onset of oxidation of cylinder-shaped Pd nanoparticles on Co_3O_4(111) to higher potentials with respect to hemisphere-shaped Pd nanoparticles on HOPG.[34] However, above the onset of oxidation, the extent of oxidation of Pd nanoparticles was considerably higher in the presence of the EMSI in the Pd/Co_3O_4(111) model system.[34]

In this paper, we systematically investigated the electrochemical stability of the monometallic Rh/Co_3O_4(111) and Pd/Co_3O_4(111) model catalysts and the bimetallic Pd–Rh core–shell nanoparticles supported on the well-ordered Co_3O_4(111) films grown on Ir(100) as a function of chemical composition and the nature of the metal/oxide interface. Towards this aim, we monitored the oxidation states of Rh, Pd and Co atoms before and after potential cycling under the conditions relevant for the electrochemical oxidation of ethanol by means of synchrotron radiation photoelectron spectroscopy coupled with an *ex situ* electrochemical cell (EC-SRPES). Our findings reveal the critical role of the EMSI in stabilizing the bimetallic core–shell nanoparticles in electrochemical environment and provide valuable insights into the related phenomena.

Experimental

Synchrotron radiation photoelectron spectroscopy coupled with an *ex situ* emersion electrochemical cell (EC-SRPES)

The high-resolution SRPES experiments were performed at the Materials Science Beamline (MSB), Elettra synchrotron light facility in Trieste, Italy. The MSB was equipped with a bending magnet source and provided synchrotron light in the energy range of 22–1000 eV. The UHV end-station (base pressure 2×10^{-10} mbar) was equipped with an electron energy analyzer (Specs Phoibos 150) with a delayline detector, a dual Mg/Al X-ray source, a rear-view LEED optics, a sputter gun (Ar^+), and a gas inlet system. In addition, an electron-beam evaporator for Co metal deposition and an electron-beam dual evaporator for Rh and Pd metals deposition were installed. The sample temperature was controlled by a DC power supply that passed current through Ta wires holding the sample. The temperature was monitored by a K-type thermocouple spot-welded to the side of the sample.

The Co_3O_4(111) film was prepared on Ir(100) based on a multi-step procedure[35–37] that has been used in other works.[32–34] The Ir(100) single crystal (MaTecK, 99.99%) was first cleaned by Ar^+ sputtering (300 K, 60 min), followed by annealing in UHV (3 min), then in an oxygen atmosphere (1×10^{-7} mbar, SIAD, 99.999%, 3 min), and again in UHV (3 min) at 1200 K until no traces of carbon or other impurities were found in the photoelectron spectra and a sharp Ir(100) (5 × 1) pattern was observed by LEED. Subsequent annealing of the Ir (100) crystal in an oxygen atmosphere (5×10^{-7} mbar, 1200 K, 5 min) yielded the (2 × 1)–O reconstruction. An epitaxial Co_3O_4(111) film was then grown on the (2 × 1)–O/Ir(100) surface by PVD of Co metal (Goodfellow, 99.99%) in an oxygen atmosphere (2×10^{-6} mbar) at 273 K, followed by annealing in oxygen (2×10^{-6} mbar) at 523 K for 20 min, followed by annealing in UHV at 680 K for 3 min. This method yielded a continuous, stoichiometric Co_3O_4(111) film with a thickness of 6.0 nm, as determined from the attenuation of the Ir 4f core level intensity. LEED observations on the prepared films confirmed the epitaxial growth of Co_3O_4(111) (see Fig. 1a).

The monometallic Pd/Co_3O_4(111) and Rh/Co_3O_4(111) model catalysts were prepared by PVD of Pd (MaTecK, 99.9%) and Rh (Goodfellow, 99.9%) metals, respectively, on Co_3O_4(111)/Ir(100) at 300 K in UHV. The nominal thicknesses of the Pd and Rh films, determined from the attenuation of the Co 2p core level intensity, were 0.39 nm and 0.42 nm, respectively. The Pd and Rh thicknesses, expressed in terms of monolayers (ML), were 1.73 ML and 1.92 ML, respectively, where 1 ML corresponds to 0.225 nm (Pd) and 0.219 nm (Rh).

The bimetallic Pd–Rh core–shell nanoparticles were prepared by subsequent PVD of 1 ML of Pd and 1 ML of Rh metals, or *vice versa*, on Co_3O_4(111)/Ir(100) at 300 K in UHV. We denote the resulting core–shell nanoparticles as Pd@Rh/Co_3O_4(111) and Rh@Pd/Co_3O_4(111) based on the broadly accepted definition for the core@shell nanoparticles, where the core is an inner metal and the shell is an outer metal.[38] The nominal thickness of the core metal was determined from the attenuation of the Co 2p core level intensity, while the nominal thickness of the shell metal was determined from the attenuation of the core level intensity of the core metal.

A specially designed EC cell was connected to the analysis chamber *via* a buffer chamber and a load lock system. The setup allowed sample transfer between the EC cell and the analysis chamber without exposure to air. A detailed description of the EC setup can be found in our previous publi-

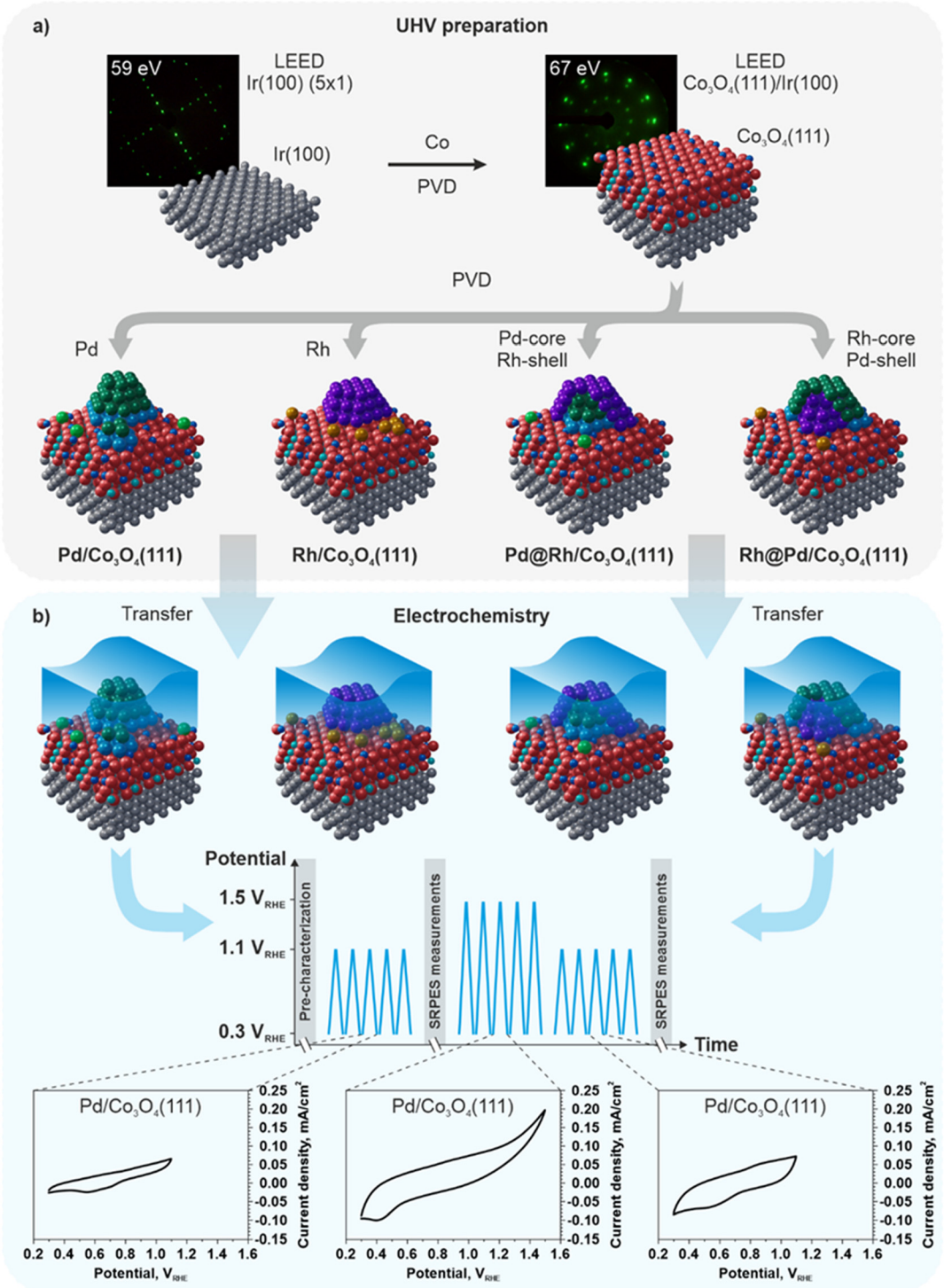

Fig. 1 Schematic representation of the preparation and treatment of the monometallic $Pd/Co_3O_4(111)$, $Rh/Co_3O_4(111)$ and bimetallic core@shell $Pd@Rh/Co_3O_4(111)$, $Rh@Pd/Co_3O_4(111)$ model systems. The preparation (a) and the cyclic voltammetry series (b). The examples of cyclic voltammograms obtained from the $Pd/Co_3O_4(111)$ (b). The ball models represent the morphology of the model catalysts. Light green, cyan, and dark green balls represent Pd^{2+}_{sol}, $Pd^{\delta+}$, and Pd^0 atoms, respectively; orange and purple balls represent Rh^{3+} and Rh^0 atoms, respectively; red, blue, and turquoise balls represent O^{2-}, Co^{2+}, and Co^{3+} ions in $Co_3O_4(111)$ film, and grey balls represent Ir in Ir(100) substrate.

cation.[29] We used the sample, a gold wire (HMW Hauner, 99.99%), and a commercial Ag/AgCl (ALS, 3 M NaCl, 0.195 V_{NHE}) as the working electrode (WE), counter electrode (CE), and reference electrode (RE), respectively. All glassware, Teflon equipment, and gold wire were soaked overnight in a solution of Nochromix (Sigma-Aldrich) and concentrated sulfuric acid

(Merck, EMSURE, 98%). Prior to the experiment, all equipment was rinsed five times with ultrapure water (Milli-Q Synergy UV, 18.2 MΩ cm at 25 °C, TOC < 5 ppb) and then boiled three times in Milli-Q water for 30 min. Gold wire was annealed in the flame of a Bunsen burner and then rinsed with ultrapure water.

The EC voltammograms were acquired upon immersion of the samples in 0.2 M ethanol (C_2H_5OH, Merck LiChrosolv, 99.9%) containing aqueous (Milli-Q Synergy UV, 18.2 MΩ cm at 25 °C, TOC < 5 ppm) electrolyte of 0.1 M potassium phosphate buffer (K_2HPO_4, Merck Suprapur, 99.99%; KH_2PO_4, Merck Suprapur, 99.99%; KOH, Alfa-Aesar, 99.98%) at pH 10. Prior to the experiment, the electrolyte was thoroughly degassed with Ar (Linde, 6.0). The EC measurement was performed by establishing a constant flow of electrolyte at the top of the capillary in the EC cell. The sample was then moved to the capillary under potential control and brought into contact with the electrolyte in a hanging meniscus geometry. The sample was then treated under the conditions of the EC experiments specified below. The potentials were controlled using a potentiostat Gamry Reference 600. The scan rate for all voltammograms was 20 mV s^{-1}. After emersion, the sample was retracted, rinsed with degassed ultrapure water, and transferred to the analysis chamber for SRPES characterization.

Core level spectra were obtained at photon energies of 410 eV (C 1s, Pd 3d, Rh 3d), 550 eV (Pd 3d, Rh 3d), 650 eV (O 1s, Pd 3d, Rh 3d), 810 eV (Pd 3d, Rh 3d), and 930 eV (Pd 3d, Rh 3d). Valence band spectra were acquired at photon energies of 60 eV and 115 eV. In addition, Al Kα radiation (1486.6 eV) was used to measure the Co 2p and Ir 4f core levels. The binding energies in the spectra were calibrated with respect to the Fermi level. All spectra were acquired with a constant pass energy and an emission angle of the photoelectrons of 0° or 20° with respect to the sample normal while using synchrotron radiation or the X-ray source, respectively.

The total spectral resolution values were 200 meV (60–115 eV), 350 meV (410 eV), 500 meV (550 eV), 650 meV (650 eV), 850 meV (810 eV), and 1 eV (930 eV). The KolXPD fitting software was used to process the obtained data and analyze the spectra.[39] The spectral components in the Pd 3d and Rh 3d core level spectra were fitted with an asymmetric Doniach–Šunjić function convoluted with a Gaussian profile after subtraction of the Shirley background. The Pd 3d and Rh 3d core level spectra were fitted using a spin–orbit splitting of 5.3 and 4.7 eV, respectively. A fixed branching ratio of 1.5 was used for the Pd 3d core level spectra. The Coster–Kronig effect, which leads to a broadening of the Rh $3d_{3/2}$ component compared to Rh $3d_{5/2}$, was considered in the fitting of the spectra. Specifically, the Rh 3d core levels were fitted with two asymmetric Doniach–Šunjić functions convoluted with a Gaussian profile, keeping the branching ratio between the peak areas at 1.5. The selected fitting parameters for Pd 3d and Rh 3d spectra obtained from as-prepared model systems are given in ESI, section S1.† The Co^{3+}/Co^{2+} concentration ratio of the $Co_3O_4(111)$ was determined from the intensities of the corresponding Co^{3+} and Co^{2+} features in the valence band spectra obtained with high surface sensitivity. More details about this method are given elsewhere.[32,40]

Scanning tunnelling microscopy (STM)

The STM and X-ray photoelectron spectroscopy (XPS) experiments were performed in an UHV system (base pressure 1×10^{-10} mbar) at the Charles University, Prague, Czech Republic. The chamber was equipped with a photoelectron spectrometer (Specs Phoibos 150), an Al Kα X-ray source, LEED, and a home-built STM. The samples were heated radiatively.

Well-ordered $Co_3O_4(111)$ thin films were grown on a clean Ir(100) substrate (MaTecK). The clean (5 × 1)–Ir(100) surface was obtained by repeated cycles of ion sputtering followed by annealing at 1330 K in UHV for 3 min, than in 1×10^{-7} mbar O_2 for 3 min, and, finally, in UHV for 3 min. Afterwards, the (5 × 1) reconstruction was lifted by annealing at 1270 K in a background pressure of 5×10^{-7} mbar O_2 (Linde, 99.999%) yielding the (2 × 1)–O/Ir(100) structure. Co (Alfa Aesar, 99.995%) was deposited onto (2 × 1)-O/Ir(100) in the background O_2 atmosphere of 1.5×10^{-6} mbar at 300 K from an electron-heated Ta crucible. After Co deposition, the layer was further oxidized in 2×10^{-6} mbar of O_2 for 60 min at 680 K. To achieve the final $Co_3O_4(111)$ ordering, annealing in UHV at 720 K was performed. The layers were prepared with a nominal thickness of approximately 5.0 nm as determined by a quartz crystal microbalance (QCM) and by attenuation of the Ir 4f XPS signal. The crystallinity of the $Co_3O_4(111)$ films was verified by means of LEED and STM (ESI, section S2†). The Rh/$Co_3O_4(111)$, Pd/$Co_3O_4(111)$, Rh@Pd/$Co_3O_4(111)$, and Pd@Rh/$Co_3O_4(111)$ model systems were prepared by the deposition of Rh and Pd metals on the as-prepared $Co_3O_4(111)$ film from the electron-heated Rh and Pd wires (Goodfellow, 99.99%) in UHV at 300 K. The nominal thickness of the deposited Rh, Pd, Rh@Pd, and Pd@Rh films was determined by means of a QCM. Specifically, the nominal thicknesses of Rh and Pd films in the Rh/$Co_3O_4(111)$ and the Pd/$Co_3O_4(111)$ model systems were 0.42 nm and 0.43 nm, respectively, which corresponds to 1.9 ML coverage for both systems. The nominal thicknesses of the core and shell metals in the Rh@Pd/$Co_3O_4(111)$ were 0.17 nm and 0.19 nm, respectively. The nominal thicknesses of the core and shell metals in the Pd@Rh/$Co_3O_4(111)$ were 0.19 nm and 0.17 nm, respectively. STM imaging was performed at 300 K using electrochemically etched W tips. STM images were obtained at tunneling voltages and currents of 2.0 V and 0.2–0.35 nA, respectively.

Results and discussion

We investigated the electrochemical stabilities of the monometallic Pd and Rh nanoparticles and bimetallic Pd@Rh and Rh@Pd core@shell nanoparticles supported on the $Co_3O_4(111)$ films epitaxially grown on the Ir(100) single crystal substrate following a model approach. The concept is based on the preparation of the well-defined model systems under UHV conditions followed by treatment under electrochemical

conditions in alkaline electrolyte (phosphate buffer pH 10) containing 0.2 M ethanol. The schematic representation of the corresponding research strategy is summarized in Fig. 1.

The well-defined model systems are shown schematically in Fig. 1a. The detailed description of the preparation procedures is given in Experimental. The analysis of the electronic structure and morphology of the model systems requires analytical methods which provide high surface sensitivity.[41] Methods based on X-ray or electron beam transmission are not suitable due to the low noble metal content and the presence of the bulk metal single crystal substrates. After preparation, the model systems were subjected to the SRPES characterization before and after the series of cyclic voltammetry (CV) procedures in 0.2 M ethanol solution in phosphate buffer (pH 10). The experimental approach is schematically shown in Fig. 1b. The first CV series involved 5 cyclic voltammograms in a potential range of 0.3–1.1 V_{RHE}. This potential range is based on the stability region of $Co_3O_4(111)$[42] and Pd nanoparticles[34] with respect to dissolution and oxidation and represents the typical potential range for ethanol oxidation.[43] The second CV series involved 5 voltammograms in the potential range of 0.3–1.5 V_{RHE} followed by 5 voltammograms in the range of 0.3–1.1 V_{RHE}. Typical voltammograms obtained in the potential regions of 0.3–1.1 V_{RHE} and 0.3–1.5 V_{RHE} during the first and the second CV series obtained from the $Pd/Co_3O_4(111)$ model system are shown in Fig. 1b. Note that the potential range of 0.3–1.5 V_{RHE} includes the regions of partial hydroxylation of $Co_3O_4(111)$[44] and Pd oxidation.[34] Therefore, cycling in the potential range of 0.3–1.5 V_{RHE} involves reversible oxidation and reduction of the catalyst which may potentially trigger restructuring,[25,27] chemical reordering in the supported nanoparticles,[27] as well as partial dissolution of the noble metals.[26] Note that $Co_3O_4(111)$ film is stable with respect to dissolution in the ranges of both CV series with the rates of Co dissolution well below the detection limit of inductively coupled plasma-mass spectrometry (ICP-MS).[29,42]

Stability of monometallic Pd and Rh nanoparticles supported on well-ordered $Co_3O_4(111)$ films

The Pd 3d and Rh 3d spectra, the integrated Pd 3d and Rh 3d intensities, and the Co^{3+}/Co^{2+} ratios obtained from the monometallic $Pd/Co_3O_4(111)$ and $Rh/Co_3O_4(111)$ model catalysts are plotted as a function of the experimental procedure in Fig. 2. The Pd 3d and Rh 3d spectra obtained from as-prepared $Pd/Co_3O_4(111)$ and $Rh/Co_3O_4(111)$ systems are shown as bottom spectra in Fig. 2a and b, respectively. The main spectral contributions in both Pd 3d and Rh 3d spectra at 335.3 eV (Pd $3d_{5/2}$) and 307.1 eV (Rh $3d_{5/2}$) arise due to the growth of metallic Pd^0 and Rh^0 nanoparticles.[33]

The EMSI in both systems yields a minor fraction of oxidized species incorporated in the oxide or at the metal/oxide interface.[32,33] Earlier, we identified the partially oxidized $Pd^{\delta+}$ aggregates in combination with PdO_x clusters and atomically dispersed $Pd^{2+}{}_{sol}$ species in the $Pd/Co_3O_4(111)$ system,[32] and atomically dispersed Rh^{3+} species in the $Rh/Co_3O_4(111)$ system.[33] Typically, the $Pd^{\delta+}/Pd^{2+}$ aggregates and atomically dispersed $Pd^{2+}{}_{sol}$ species are strongly attenuated by metallic Pd^0 nanoparticles at high coverages.[32] As a result, these species are hardly visible in the Pd 3d spectra obtained with surface sensitive photon energies (see Fig. 2a, bottom spectrum) but can be still detected using higher photon energies[32] (see ESI, section S3†). In contrast, the contribution from atomically dispersed Rh^{3+} species is well-resolved in the Rh 3d spectrum at 308.2 eV (Rh $3d_{5/2}$). The STM images obtained from the $Pd/Co_3O_4(111)$ and $Rh/Co_3O_4(111)$ model systems revealed the growth of well-dispersed Pd and Rh nanoparticles (Fig. 2, side panels). In our previous studies we investigated the morphologies of the Pd and Rh nanoparticles in a great detail.[32,33] Basically, both Pd and Rh nanoparticles acquire cylindrical shapes on $Co_3O_4(111)$, but differ strongly with respect to the average size and the density of supported nanoparticles. Specifically, Pd nanoparticles have average diameter of 5–6 nm and the particle density of 2.7×10^{12} cm^{-2}. In contrast, the Rh nanoparticles have an average diameter of 3.3 nm and the particle density is 7.3×10^{12} cm^{-2}. The observed morphologies are consistent with different magnitude of the EMSI in two systems.[33] Namely, the larger magnitude of the EMSI in $Rh/Co_3O_4(111)$ model system yields the nanoparticles of smaller size at higher particle density with respect to the $Pd/Co_3O_4(111)$ model system. Nevertheless, the heights of the Pd and Rh nanoparticles are similar, *i.e.* 3–4 ML.[33] Note that the height is the most important parameter determining the extent of oxidation of the Pd nanoparticles supported on $Co_3O_4(111)$ under electrochemical conditions.[34]

After the first CV series, we observed a decrease in the total intensity of the Pd 3d spectra (Fig. 2a, middle spectrum and Fig. 2c) accompanied by a shift of the metallic Pd^0 contribution by 0.3 eV toward higher binding energies. After the second CV series, we observed much stronger decrease of the Pd 3d intensity (Fig. 2a, top spectrum and Fig. 2c). The corresponding shift of the Pd^0 contribution can be explained by adsorption of carbonaceous residues after electrochemical experiments.[34] However, the decrease of the total Pd 3d intensity after the first and the second CV series cannot be explained solely in terms of the attenuation. In particular, the loss of Pd due to dissolution in electrolyte has to be taken into consideration. Towards this aim, we performed the analysis of the total Pd 3d intensities obtained with different photon energies before and after CV series (SRPES method, see ESI, section S4†). We validated the SRPES method based on the comparison of the amounts of dissolved noble metal determined by SRPES and online ICP-MS using identical samples subjected to similar electrochemical treatments. The fraction of dissolved metal was calculated using a Python script (see ESI, section S4†). The corresponding approach allowed us to estimate the thickness of the carbonaceous deposits and the amount of dissolved Pd. We estimated that about 7% of Pd is dissolved into electrolyte and about 0.31 nm thick amorphous carbon layer is deposited onto Pd nanoparticles after the first CV series. After the second CV series, 20–25% of Pd is dissolved and 0.52 nm of amorphous carbon film is deposited onto Pd nanoparticles with respect to as-prepared system.

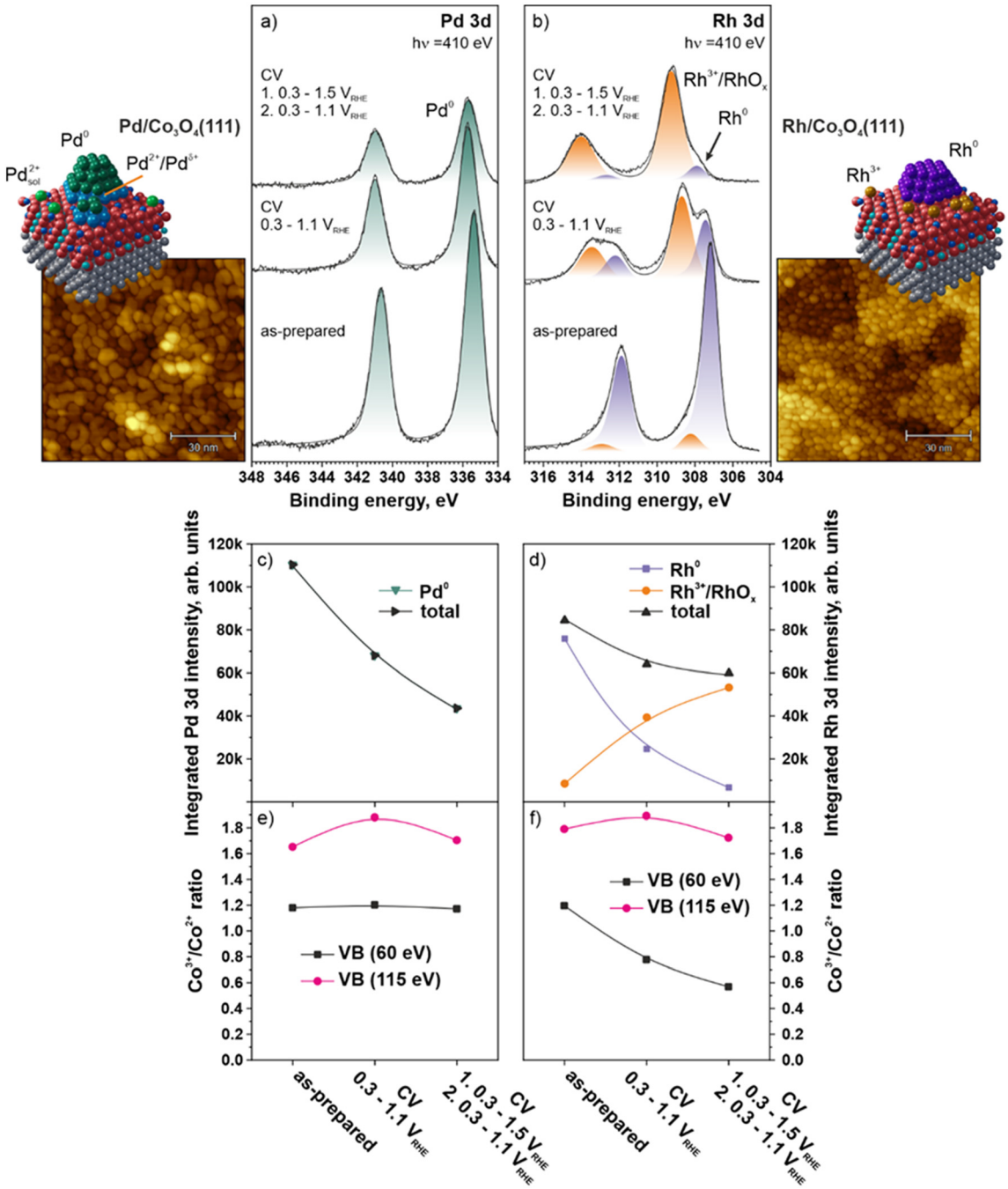

Fig. 2 Pd 3d (a) and Rh 3d (b) core level spectra, the evolution of the integrated Pd 3d intensities of the Pd surface species (c) and of the integrated Rh 3d intensities of the Rh surface species (d), and the evolution of the Co^{3+}/Co^{2+} ratios (e and f) obtained from Pd/Co_3O_4(111) (a, c and e) and Rh/Co_3O_4(111) (b, d and f) model catalysts before and after electrochemical experiments. The Pd 3d and Rh 3d spectra were acquired with photon energies of 410 eV. The STM images obtained from the 1.9 ML Pd/Co_3O_4(111) (left panel) and 1.9 ML Rh/Co_3O_4(111) (right panel) model catalysts at 300 K.

Stronger dissolution of Pd after the second CV series is consistent with a larger extent of Pd oxidation due to cycling in the range of 0.3–1.5 V_{RHE}. Earlier we have shown that Pd nanoparticles are strongly oxidized at 1.5 V_{RHE} due to the EMSI effect.[34] Nevertheless, the absence of stable palladium oxides in the Pd 3d spectra after the first and the second CV series suggests that the reversible oxidation/reduction of Pd is a fast process and the metallic state is fully recovered after cycling.

Interestingly, we observed very different behavior in the Rh/Co_3O_4(111) model systems under similar conditions. After the first CV series, the oxidized Rh contribution increased strongly at the expense of the metallic Rh^0 contribution (Fig. 2b,

middle spectrum and Fig. 2d). In addition, the binding energies of the oxidized and metallic Rh^0 contributions shifted by 0.5 and 0.3 eV, respectively, toward the higher binding energy. These shifts were not accompanied by the shifts of the Co 2p or O 1s contributions (see ESI, section S5†). After the second CV series, we observed further oxidation of Rh and a shift of the oxidized and metallic Rh^0 contributions to 309.3 eV (Rh $3d_{5/2}$) and 307.9 eV (Rh $3d_{5/2}$), respectively. Noteworthy, the shift of the oxidized Rh 3d contribution is about 1.0 eV with respect to the corresponding Rh 3d component in as-prepared $Rh/Co_3O_4(111)$ system. However, at this time, the shift of the oxidized Rh contribution is accompanied by the similar shifts of the Co 2p and O 1s core level spectra (see ESI, section S5†). Generally, this observation suggests a different nature of the oxidized Rh species formed after the first and the second CV series. In this respect, similar shifts of the oxidized Rh 3d and Co 2p and O 1s contributions suggests that oxidized Rh species got integrated into the $Co_3O_4(111)$ substrate. Note, if oxidized Rh 3d contribution is not accompanied with a similar shifts of the Co 2p and O 1s, it means that oxidized Rh is decoupled from the $Co_3O_4(111)$ substrate.

With respect to the nature of the oxidized Rh species formed after the first and the second CV series, we refer to the Pourbaix diagram.[26] Accordingly, the formation of stable Rh_2O_3 takes place in the potential range of 0.84–1.79 V_{RHE} in alkaline electrolyte, whereas RhO_2 forms above 1.79 V_{RHE}.[26] Taking into account the chemical shifts, we assume that after the first CV series, Rh nanoparticles are oxidized at the top forming a Rh_2O_3-like oxide. In contrast, the oxidized Rh species formed after the second CV series represent atomically dispersed Rh^{3+} species anchored at the $Co_3O_4(111)$ substrate in combination with some Rh_2O_3-like oxide. We note that the Rh^{3+} species in the form of Rh_2O_3-like oxide and the Rh^{3+} species anchored at the $Co_3O_4(111)$ substrate cannot be resolved reliably due to the similar binding energies.[33,45] Therefore, we label the corresponding contributions as Rh^{3+}/RhO_x.

Finally, we associate the binding energy shifts of the Rh^0 contribution after the first and the second CV series to a particle size effect.[46,47] This assignment is consistent with the decreasing size of metallic Rh^0 core due to oxidation or disintegration and anchoring of Rh^{3+} and formation of RhO_x species on the $Co_3O_4(111)$ substrate. Most interestingly, despite the strong oxidation, the decrease of the total intensity of the Rh 3d spectra after the first and the second CV series is rather small. However, we cannot estimate the extent of Rh dissolution in the $Rh/Co_3O_4(111)$ system due to unknown morphology of the catalyst after CV series. Still, based on the total Rh 3d intensities, we conclude that the extent of Rh dissolution is considerably smaller in comparison to the $Pd/Co_3O_4(111)$ system.

With respect to the EMSI in the $Pd/Co_3O_4(111)$ and $Rh/Co_3O_4(111)$ model systems, we analyzed the oxidation state of the $Co_3O_4(111)$ support. The Co^{3+}/Co^{2+} ratios calculated from the heights of the corresponding Co^{3+} and Co^{2+} features in the valence bands obtained with photon energy of 60 and 115 eV are shown in Fig. 2e and f. Note that the Co^{3+}/Co^{2+} ratios obtained with photon energy of 60 and 115 eV correspond to the surface and sub-surface sensitivities, respectively, due to the different inelastic mean free paths (IMFP) of the corresponding photoelectrons.[48] The most important differences between the $Pd/Co_3O_4(111)$ and the $Rh/Co_3O_4(111)$ model systems concern the evolution of the Co^{3+}/Co^{2+} ratios obtained with the highest surface sensitivity (photon energy 60 eV). First, in both as-prepared systems, the Co^{3+}/Co^{2+} ratios are similar. This suggests a similar magnitude of the charge transfer at the metal/oxide interface which corresponds roughly to the reduction of 50% of Co^{3+} cations in the second cationic layer of the $Co_3O_4(111)$ substrate.[32] Interestingly, the Co^{3+}/Co^{2+} ratio remains virtually unchanged on $Pd/Co_3O_4(111)$ after the first and the second CV series. In contrast, the Co^{3+}/Co^{2+} ratio significantly decreases for $Rh/Co_3O_4(111)$ after the first and the second CV series. The total drop of the Co^{3+}/Co^{2+} ratio by as much as a factor of 2 in $Rh/Co_3O_4(111)$ corresponds to the reduction of nearly 100% of the Co^{3+} cations in the second cationic layer of the $Co_3O_4(111)$ substrate.[32] The observed differences in the evolution of the Co^{3+}/Co^{2+} ratios in two model systems suggest that the $Co_3O_4(111)$ substrate actively participates in anchoring of the oxidized Rh species and, thus, prevents Rh dissolution into electrolyte. Nevertheless, based on the comparison of the Co^{3+}/Co^{2+} ratios obtained with different photon energies, we assume that the reduction of $Co_3O_4(111)$ is limited to the surface, while the sub-surface region remains nearly unaffected. This observation suggests that the structure of the $Co_3O_4(111)$ film is largely preserved during cycling.

Additionally, we explored the depth distribution of the Rh species in the $Rh/Co_3O_4(111)$ model system by the analysis of the Rh 3d spectra obtained with different photon energies between 410 and 930 eV (see ESI, section S6 and Fig. S6†). We verified that after the first CV series, the RhO_x species are distributed at the surface and cover the metallic Rh^0 nanoparticles. In contrast, after the second CV series, both the oxidized and metallic Rh^0 species are distributed at the surface and do not attenuate the contributions of each other.

Stability of Rh@Pd and Pd@Rh core@shell nanoparticles supported on well-ordered $Co_3O_4(111)$ films

The Rh 3d and Pd 3d spectra, the integrated Rh 3d and Pd 3d intensities, and the Co^{3+}/Co^{2+} ratios obtained from the $Rh@Pd/Co_3O_4(111)$ and $Pd@Rh/Co_3O_4(111)$ core@shell model systems are plotted for the same experimental procedure in Fig. 3 and 4, respectively. First, we focus on the $Rh@Pd/Co_3O_4(111)$ model system where the Rh-core is in direct contact with the $Co_3O_4(111)$ substrate (Fig. 3). The Rh 3d and Pd 3d spectra obtained from as-prepared $Rh@Pd/Co_3O_4(111)$ model system are shown as bottom spectra in Fig. 3a and b, respectively.

The dominant species in both the Rh-core and Pd-shell are metallic Rh^0 and Pd^0 associated with the main contributions at 307.1 eV (Rh $3d_{5/2}$) and 335.3 eV (Pd $3d_{5/2}$), respectively. A minor contribution from the atomically dispersed Rh^{3+} emerges at 308.2 eV (Rh $3d_{5/2}$). The STM image obtained from

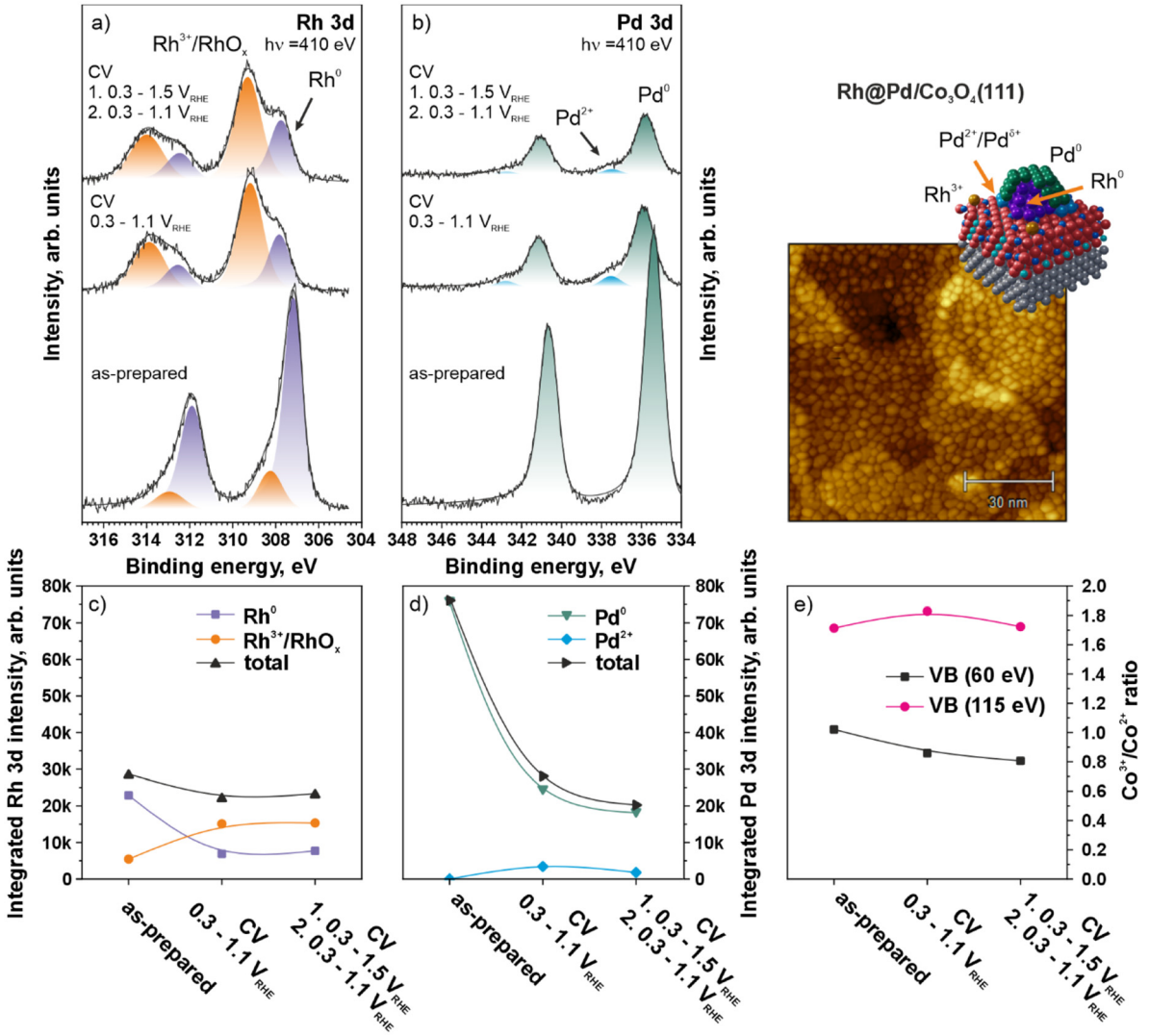

Fig. 3 Rh 3d (a) and Pd 3d (b) core level spectra, the evolution of the integrated Rh 3d (c) and Pd 3d (d) intensities of the surface species, and the evolution of the Co^{3+}/Co^{2+} ratio (e) obtained from the Rh@Pd/Co_3O_4(111) model catalyst before and after electrochemical experiments. The STM image obtained from the Rh@Pd/Co_3O_4(111) model system at 300 K.

the as-prepared Rh@Pd/Co_3O_4(111) model system reveals formation of nanoparticles. Earlier, we characterized the morphology of supported Rh@Pd nanoparticles in a great detail.[33] We found that the average diameter of the Rh@Pd nanoparticles is 3.0 nm and the density is 7.7×10^{12} cm^{-2}. The observed morphology of the Rh@Pd nanoparticles is similar to the one observed for monometallic Rh nanoparticles. Surprisingly, already after the first CV series, we observed substantial binding energy shifts of the Rh^0 and oxidized Rh contributions by 0.7 and 1.0 eV toward higher binding energies, reaching 307.8 eV (Rh $3d_{5/2}$) and 309.2 eV (Rh $3d_{5/2}$), respectively. In the Pd 3d spectrum, a minor contribution from the Pd^{2+} state at 337.5 eV (Pd $3d_{5/2}$) appeared together with a 0.5 eV shift in the binding energy of the Pd^0 contribution toward higher binding energies. Noteworthy, the shift of the oxidized Rh contribution is accompanied by similar shifts of the Co 2p and O 1s core levels (see ESI, section S5†). This observation suggests atomic dispersion and anchoring of the oxidized Rh^{3+} species on the Co_3O_4(111) substrate already after the first CV series. This suggestion is in line with the decrease of the Co^{3+}/Co^{2+} ratios (Fig. 3e).

After the second CV series, no changes in the oxidation state of the Rh@Pd/Co_3O_4(111) model system were observed. The observed scenario suggests that the Rh@Pd/Co_3O_4(111) model system is more prone to oxidation than the monometallic Rh/Co_3O_4(111) and Pd/Co_3O_4(111) model systems. With respect to the total Rh 3d and Pd 3d intensities, we found that the Rh 3d intensity decrease is minor, whereas the Pd 3d intensity decreases significantly after the first and the second CV series. This observation suggests that the dissolution of the Rh-core is significantly suppressed whereas Pd-shell is prone to dissolution. We performed a similar analysis of the total Pd

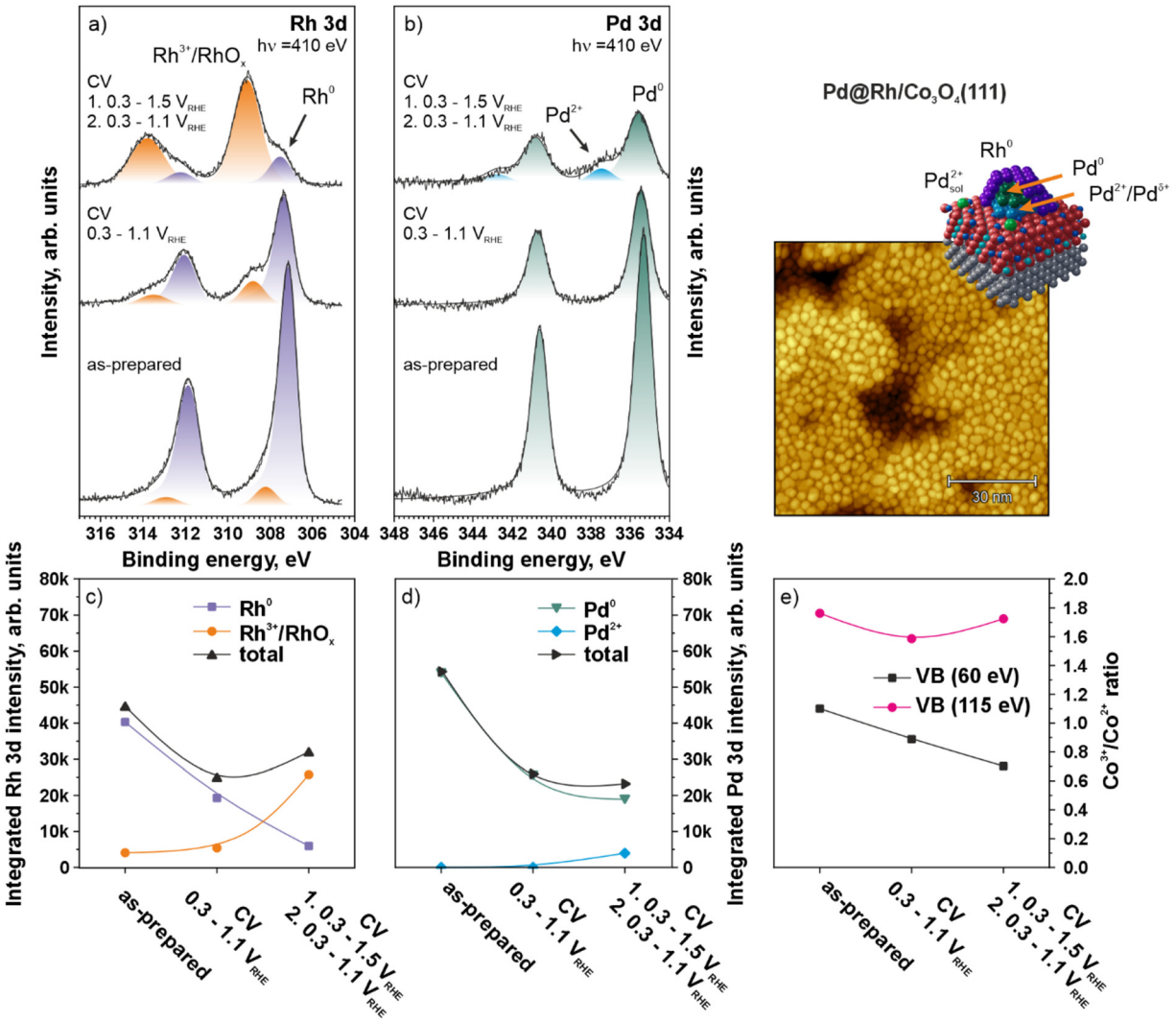

Fig. 4 Rh 3d (a) and Pd 3d (b) core level spectra, the evolution of the integrated Rh 3d (c) and Pd 3d (d) intensities of the surface species, and the evolution of the Co^{3+}/Co^{2+} ratio (e) obtained from the Pd@Rh/Co_3O_4(111) model catalyst before and after electrochemical experiments. The STM image obtained from the Pd@Rh/Co_3O_4(111) model system at 300 K.

3d intensities as in the case of monometallic Pd/Co_3O_4(111) (see ESI, section S4†). We estimated that about 30% and 50% of Pd-shell dissolves into electrolyte after the first and the second EC series, respectively. The analysis of the depth distribution of the Rh species in the Rh@Pd/Co_3O_4(111) model system revealed that the Rh^{3+} species are located mainly at the surface of the catalyst (see ESI, section S6 and Fig. S7†).

Finally, we focus on the Pd@Rh/Co_3O_4(111) model system, where Pd@Rh core@shell nanoparticles have the Pd-core in the direct contact with the Co_3O_4(111) substrate (Fig. 4). The Rh 3d and Pd 3d spectra obtained from the as-prepared Pd@Rh/Co_3O_4(111) model system are shown as bottom spectra in Fig. 4a and b, respectively. The dominant species in both the Pd-core and Rh-shell are metallic Pd^0 and Rh^0 that give rise to the main contributions at 335.3 eV (Pd $3d_{5/2}$) and 307.1 eV (Rh $3d_{5/2}$), respectively. A minor contribution from the atomically dispersed Rh^{3+} emerges at 308.2 eV (Rh $3d_{5/2}$). The STM image obtained from the as-prepared Pd@Rh/Co_3O_4(111) model system reveals formation of nanoparticles. Earlier, we characterized the morphology of supported Pd@Rh nanoparticles in great detail.[33] Generally, we found that the average diameter and the density of the Pd@Rh nanoparticles are identical to these observed for Rh@Pd nanoparticles, which correspond to 3.0 nm and the density is 7.7×10^{12} cm^{-2}, respectively.

However, in contrast to the Rh@Pd/Co_3O_4(111) model system, we observed a significant suppression of oxidation of both Pd-core and Rh-shell after the first CV series. Still, the Rh^0 and oxidized Rh contributions shifted by 0.2 and 0.6 eV toward higher binding energies, reaching 307.3 eV (Rh $3d_{5/2}$) and 308.8 eV (Rh $3d_{5/2}$), respectively. The Pd^0 contribution shifted by 0.1 eV toward higher binding energies. Noteworthy, the shift of the oxidized Rh contribution is not accompanied by similar shifts of the Co 2p and O 1s contributions (see ESI,

section S5†). Therefore, in correspondence with our previous observation discussed above, we associate the corresponding scenario with the formation of RhO_x which is predominantly not in contact with $Co_3O_4(111)$. Nevertheless, the decrease of the Co^{3+}/Co^{2+} ratio suggests that a fraction of oxidized Rh species must be also anchored at the $Co_3O_4(111)$ surface (Fig. 4e). Most importantly, we relate the significant suppression of oxidation of Rh-shell to the lower magnitude of the EMSI due to decoupling of Rh and $Co_3O_4(111)$ at the interface using the metallic Pd-core as a buffer layer.

After the second CV series, we observed a significant increase of the oxidized Rh contribution at the expense of the Rh^0 contribution accompanied by its shift to 309.1 eV (Rh $3d_{5/2}$). In addition, a minor contribution of Pd^{2+} at 337.5 eV (Pd $3d_{5/2}$) appeared in the Pd 3d spectrum. Noteworthy, the shift of the oxidized Rh component is accompanied by smaller shifts of the Co 2p and O 1s contributions (see ESI, section S5†). Still, we observed a further decrease of the Co^{3+}/Co^{2+} ratio, suggesting an increase in the fraction of oxidized Rh species anchored at the $Co_3O_4(111)$ surface (Fig. 4e). This observation suggests the predominant formation of RhO_x over the Pd-core and partial anchoring of Rh^{3+} species at the surface of $Co_3O_4(111)$. Additionally, we attribute the appearance of the Pd^{2+} contribution to the formation of PdO oxide.

With respect to the dissolution of the Pd@Rh nanoparticles, we observed a decrease in the total Rh 3d and Pd 3d intensities by a factor of 2 only after the first CV series. After the second CV series, the total intensity of the Rh 3d core level slightly increased, while the total Pd 3d intensity remain virtually unchanged. We speculate that the effect is caused by a slight expansion of the Rh-shell due to oxidation and distribution of the Rh^{3+} over the surface of $Co_3O_4(111)$.

The analysis of the depth distribution of the Rh species in the Pd@Rh/$Co_3O_4(111)$ model system revealed that the oxidized Rh species are located at the surface of the catalyst (see ESI, section S6 and Fig. S8†).

Conclusions

We have investigated the stability of monometallic Rh and Pd, and bimetallic Rh@Pd and Pd@Rh core@shell nanoparticles supported on well-ordered $Co_3O_4(111)$ films grown on Ir(100) with respect to the oxidation and dissolution in alkaline electrolyte under the conditions relevant for the electrochemical oxidation of ethanol. The well-defined model catalysts were systematically characterized by means of *ex situ* EC-SRPES before and after different CV series:

CV series in the range of 0.3–1.1 V_{RHE}

(a) *Monometallic Pd and Rh nanoparticles*: in the corresponding potential region, the EMSI has practically no impact on the oxidation state and dissolution of monometallic Pd nanoparticles. The supported Pd nanoparticles remain metallic but undergo minor dissolution into the electrolyte. In strong contrast, monometallic Rh nanoparticles are prone to oxidation. The supported Rh nanoparticles are partially covered by stable RhO_x. The EMSI results in anchoring of a fraction of the oxidized Rh^{3+} species at the surface of $Co_3O_4(111)$. The corresponding mechanism prevents dissolution of Rh into electrolyte.

(b) *Bimetallic Pd–Rh nanoparticles*: the EMSI has the largest impact on the Rh@Pd core@shell nanoparticles when the Rh-core is in direct contact with $Co_3O_4(111)$. It results in a strong oxidation and anchoring of a large fraction of oxidized Rh^{3+} species at the surface of the $Co_3O_4(111)$. This prevents dissolution of Rh-core into electrolyte but leads to minor oxidation and stronger dissolution of Pd-shell. The impact of the EMSI is minimized for the Pd@Rh nanoparticles, where Pd-core is in direct contact with $Co_3O_4(111)$. The Pd@Rh nanoparticles are less prone to oxidation and dissolution in comparison to the Rh@Pd nanoparticles. Specifically, Rh-shell in the Pd@Rh nanoparticles gains a higher stability with respect to oxidation in comparison to monometallic Rh nanoparticles.

CV series in the range of 0.3–1.5 V_{RHE} followed by cycling in the range of 0.3–1.1 V_{RHE}

(c) *Monometallic Pd and Rh nanoparticles*: in the corresponding potential region, the oxidation of Pd nanoparticles is reversible which results in a fast recovery of the metallic state but leads to stronger dissolution into electrolyte. In contrast, the Rh nanoparticles undergo nearly complete oxidation. The anchoring of the oxidized Rh^{3+} species at the surface of $Co_3O_4(111)$ prevents dissolution of Rh into electrolyte.

(d) *Bimetallic Pd–Rh nanoparticles*: the structure and the oxidation state of the Rh@Pd nanoparticles formed after the first CV series remains stable thereafter. The Pd@Rh nanoparticles remain stable with respect to dissolution but the Rh-shell gets strongly oxidized.

The findings of our study demonstrate the potential of the EMSI to stabilize noble metals against dissolution into electrolytes. However, it is imperative to regulate its magnitude to prevent excessive oxidation of the supported metals under electrochemical conditions. The rational design of multifunctional core@shell nanoparticles offers a promising avenue for enhancing the efficiency of noble metal utilization in electrocatalysis.

Author contributions

Alexander Simanenko: formal analysis, investigation, visualization, writing – original draft, writing – review & editing. Jan Škvára: formal analysis, investigation, visualization. Pankaj Kumar Samal: formal analysis, investigation, visualization. Evanie Franz: investigation. Robert Hübsch: investigation. Tomáš Skála: investigation, writing – review & editing. Nataliya Tsud: investigation, writing – review & editing. Sascha Mehl: investigation. Daniel Schauermann: software – programming, software development. Viktor Johánek: investigation, funding acquisition. Josef Mysliveček: funding acquisition, writing – review & editing. Olaf Brummel: funding acquisition, writing –

review & editing. Yaroslava Lykhach: conceptualization, visualization, investigation, project administration, supervision, writing – review & editing. Jörg Libuda: conceptualization, supervision, writing – review & editing, funding acquisition.

Data availability

Source data are provided at Zenodo: **https://doi.org/10.5281/zenodo.14733690**.

Conflicts of interest

There are no conflicts to declare.

Acknowledgements

The authors acknowledge financial support by the Deutsche Forschungsgemeinschaft (DFG) (project 431733372), the Czech Science Foundation (GAČR, project 20-21727X) and the Czech Ministry of Education, Youth and Sports (MŠMT, project QM4ST, reg. no. CZ.02.01.01/00/22_008/0004572). J. Š. acknowledges the support of the Grant Agency of the Charles University (GAUK, project 199423). Additional support is acknowledged by the Collaborative Research Centre SFB 1452 – Catalysis at Liquid Interfaces (project 431791331) and project 453560721. The authors acknowledge the CERIC-ERIC Consortium for access to experimental facilities and financial support. The authors also acknowledge the support by the Czech Ministry of Education, Youth and Sports (project LM2023072).

References

1 Z. Zakaria, S. K. Kamarudin and S. N. Timmiati, *Appl. Energy*, 2016, **163**, 334–342.
2 Y. Yang, P. Li, X. Zheng, W. Sun, S. X. Dou, T. Ma and H. Pan, *Chem. Soc. Rev.*, 2022, **51**, 9620–9693.
3 A. Han and G. Liu, *Mater. Chem. Front.*, 2024, **8**, 903–929.
4 J. Chang, G. Wang, X. Chang, Z. Yang, H. Wang, B. Li, W. Zhang, L. Kovarik, Y. Du, N. Orlovskaya, B. Xu, G. Wang and Y. Yang, *Nat. Commun.*, 2023, **14**, 1346.
5 T. Chen, M. Wang, D. Hu, Q. Ju, K. Zhao, L. Fu, Z. Chen, X. Yu and C. Li, *ACS Appl. Energy Mater.*, 2024, **7**, 6166–6176.
6 M. L. Weber, B. Šmíd, U. Breuer, M.-A. Rose, N. H. Menzler, R. Dittmann, R. Waser, O. Guillon, F. Gunkel and C. Lenser, *Nat. Mater.*, 2024, **23**, 406–413.
7 E. Berretti, L. Osmieri, V. Baglio, H. A. Miller, J. Filippi, F. Vizza, M. Santamaria, S. Specchia, C. Santoro and A. Lavacchi, *Electrochem. Energy Rev.*, 2023, **6**, 30.
8 P. Bishnoi, K. Mishra, S. S. Siwal, V. K. Gupta and V. K. Thakur, *Adv. Energy Sustainability Res.*, 2024, **5**, 2300266.
9 Y. Wang, S. Zou and W.-B. Cai, *Catalysts*, 2015, **5**, 1507.
10 M. A. F. Akhairi and S. K. Kamarudin, *Int. J. Hydrogen Energy*, 2016, **41**, 4214–4228.
11 J. E. Mueller, P. Krtil, L. A. Kibler and T. Jacob, *Phys. Chem. Chem. Phys.*, 2014, **16**, 15029–15042.
12 D. Wu, K. Kusada and H. Kitagawa, *Sci. Technol. Adv. Mater.*, 2016, **17**, 583–596.
13 L. Jin, H. Xu, C. Chen, H. Shang, Y. Wang and Y. Du, *Inorg. Chem.*, 2019, **58**, 12377–12384.
14 B.-Q. Miao, Z.-H. Yuan, X.-L. Liu, X. Ai, G.-T. Zhao, P. Chen, P.-J. Jin and Y. Chen, *Chin. J. Chem.*, 2024, **42**, 2633–2640.
15 Y. Xu, J. Li, M. Hu, Z. Wu and Y. Du, *Nanoscale*, 2024, **16**, 14096–14100.
16 B. Sun, W. Zhong, X. Ai, C. Zhang, F.-M. Li and Y. Chen, *Energy Environ. Sci.*, 2024, **17**, 2219–2227.
17 Q. Xue, Z. Ge, Z. Yuan, J. Huang, B. He and Y. Chen, *Mater. Today Phys.*, 2023, **31**, 100980.
18 A. V. Zeigarnik, R. E. Valdés-Pérez and O. N. Myatkovskaya, *J. Phys. Chem. B*, 2000, **104**, 10578–10587.
19 A. M. da Silva, K. R. de Souza, G. Jacobs, U. M. Graham, B. H. Davis, L. V. Mattos and F. B. Noronha, *Appl. Catal., B*, 2011, **102**, 94–109.
20 Z. Fang, J. Wang, X. Huang, M. Noroozifar and H.-B. Kraatz, *Int. J. Hydrogen Energy*, 2024, **87**, 1404–1415.
21 M. Bogar, Y. Yakovlev, D. J. S. Sandbeck, S. Cherevko, I. Matolínová, H. Amenitsch and I. Khalakhan, *ACS Catal.*, 2021, **11**, 11360–11370.
22 A. Kormanyos, P. Büttner, M. Bosch, M. Minichova, A. Körner, K. J. Jenewein, A. Hutzler, K. J. J. Mayrhofer, J. Bachmann and S. Cherevko, *ACS Mater. Au*, 2024, **4**, 286–299.
23 D. Göhl, P. Paciok, Z. Wang, J. S. Kang, M. Heggen, K. J. J. Mayrhofer, Y. Román-Leshkov and M. Ledendecker, *Nano Sel.*, 2023, **4**, 271–277.
24 T. C. Gentil, M. Minichova, V. Briega-Martos, V. S. Pinheiro, F. M. Souza, J. Paulo, C. Moura, J. C. M. Silva, B. L. Batista, M. C. Santos and S. Cherevko, *J. Catal.*, 2024, **440**, 115816.
25 S. C. S. Lai, R. A. Lazenby, P. M. Kirkman and P. R. Unwin, *Chem. Sci.*, 2015, **6**, 1126–1138.
26 M. Schalenbach, O. Kasian, M. Ledendecker, F. D. Speck, A. M. Mingers, K. J. J. Mayrhofer and S. Cherevko, *Electrocatalysis*, 2018, **9**, 153–161.
27 M. Vega-Paredes, R. Aymerich-Armengol, D. Arenas Esteban, S. Martí-Sánchez, S. Bals, C. Scheu and A. Garzón Manjón, *ACS Nano*, 2023, **17**, 16943–16951.
28 F. Faisal, C. Stumm, M. Bertram, F. Waidhas, Y. Lykhach, S. Cherevko, F. Xiang, M. Ammon, M. Vorokhta, B. Šmíd, T. Skála, N. Tsud, A. Neitzel, K. Beranová, K. C. Prince, S. Geiger, O. Kasian, T. Wähler, R. Schuster, M. A. Schneider, V. Matolín, K. J. J. Mayrhofer, O. Brummel and J. Libuda, *Nat. Mater.*, 2018, **17**, 592–598.
29 M. Bertram, C. Prössl, M. Ronovský, J. Knöppel, P. Matvija, L. Fusek, T. Skála, N. Tsud, M. Kastenmeier, V. Matolín, K. J. J. Mayrhofer, V. Johánek, J. Mysliveček, S. Cherevko, Y. Lykhach, O. Brummel and J. Libuda, *J. Phys. Chem. Lett.*, 2020, **11**, 8365–8371.

30 Y. Lykhach, F. Faisal, T. Skála, A. Neitzel, N. Tsud, M. Vorokhta, F. Dvořák, K. Beranová, Y. Kosto, K. C. Prince, V. Matolín and J. Libuda, *J. Mater. Chem. A*, 2018, **6**, 23078–23086.
31 Y. Lykhach, S. M. Kozlov, T. Skála, A. Tovt, V. Stetsovych, N. Tsud, F. Dvořák, V. Johánek, A. Neitzel, J. Mysliveček, S. Fabris, V. Matolín, K. M. Neyman and J. Libuda, *Nat. Mater.*, 2016, **15**, 284–288.
32 M. Kastenmeier, L. Fusek, F. Mohamed, C. Schuschke, M. Ronovský, T. Skála, M. Farnesi Camellone, N. Tsud, V. Johánek, S. Fabris, J. Libuda, S. Piccinin, Y. Lykhach, J. Mysliveček and O. Brummel, *J. Phys. Chem. C*, 2023, **127**, 6034–6044.
33 A. Simanenko, J. Škvára, P. K. Samal, L. Fusek, M. Kastenmeier, M. Ronovský, T. Skála, N. Tsud, S. Mehl, V. Johánek, J. Mysliveček, O. Brummel, Y. Lykhach and J. Libuda, *J. Phys. Chem. C*, 2025, **129**, 983–992.
34 M. Kastenmeier, L. Fusek, X. Deng, T. Skála, S. Mehl, N. Tsud, S. Grau, C. Stumm, V. Uvarov, V. Johánek, J. Libuda, Y. Lykhach, J. Mysliveček and O. Brummel, *J. Phys. Chem. C*, 2022, **126**, 12870–12881.
35 W. Meyer, K. Biedermann, M. Gubo, L. Hammer and K. Heinz, *J. Phys.: Condens. Matter*, 2008, **20**, 265011.
36 K. Biedermann, M. Gubo, L. Hammer and K. Heinz, *J. Phys.: Condens. Matter*, 2009, **21**, 185003.
37 K. Heinz and L. Hammer, *J. Phys.: Condens. Matter*, 2013, **25**, 173001.
38 H.-P. Feng, L. Tang, G.-M. Zeng, Y. Zhou, Y.-C. Deng, X. Ren, B. Song, C. Liang, M.-Y. Wei and J.-F. Yu, *Adv. Colloid Interface Sci.*, 2019, **267**, 26–46.
39 J. Libra, KolXPD: Spectroscopy Data Measurement and Processing, **https://www.kolibrik.net/science/kolxpd/**, (accessed 25.11.2024).
40 Y. Lykhach, S. Piccinin, T. Skála, M. Bertram, N. Tsud, O. Brummel, M. Farnesi Camellone, K. Beranová, A. Neitzel, S. Fabris, K. C. Prince, V. Matolín and J. Libuda, *J. Phys. Chem. Lett.*, 2019, **10**, 6129–6136.
41 G. Rupprechter, Surface Science Approach to Heterogeneous Catalysis, in *Surface and Interface Science*, 2016, pp. 459–528.
42 F. Faisal, M. Bertram, C. Stumm, S. Cherevko, S. Geiger, O. Kasian, Y. Lykhach, O. Lytken, K. J. J. Mayrhofer, O. Brummel and J. Libuda, *J. Phys. Chem. C*, 2018, **122**, 7236–7248.
43 Y. Guo, B. Li, S. Shen, L. Luo, G. Wang and J. Zhang, *ACS Appl. Mater. Interfaces*, 2021, **13**, 16602–16610.
44 O. Brummel, Y. Lykhach, M. Vorokhta, B. Šmíd, C. Stumm, F. Faisal, T. Skála, N. Tsud, A. Neitzel, K. Beranová, K. C. Prince, V. Matolín and J. Libuda, *J. Phys. Chem. C*, 2019, **123**, 8746–8758.
45 Y. Abe, K. Kato, M. Kawamura and K. Sasaki, *Surf. Sci. Spectra*, 2002, **8**, 117–125.
46 M. G. Mason, *Phys. Rev. B:Condens. Matter Mater. Phys.*, 1983, **27**, 748–762.
47 M. G. Mason, L. J. Gerenser and S. T. Lee, *Phys. Rev. Lett.*, 1977, **39**, 288–291.
48 S. Tanuma, C. J. Powell and D. R. Penn, *Surf. Interface Anal.*, 1994, **21**, 165–176.